BIOMATERIALS

Bioinspired design of a tissue-engineered ray with machine learning

John F. Zimmerman[1], Daniel J. Drennan[1]†, James Ikeda[1], Qianru Jin[1], Herdeline Ann M. Ardoña[1]‡, Sean L. Kim[1], Ryoma Ishii[1,2], Kevin Kit Parker[1]*

In biomimetic design, researchers recreate existing biological structures to form functional devices. For biohybrid robotic swimmers assembled with tissue engineering, this is problematic because most devices operate at different length scales than their naturally occurring counterparts, resulting in reduced performance. To overcome these challenges, here, we demonstrate how machine learning–directed optimization (ML-DO) can be used to inform the design of a biohybrid robot, outperforming other nonlinear optimization techniques, such as Bayesian optimization, in the selection of high-performance geometries. We show how this approach can be used to maximize the thrust generated by a tissue-engineered mobuliform miniray. This results in devices that can swim at the millimeter scale while more closely preserving natural locomotive scaling laws. Overall, this work provides a quantitatively rigorous approach for the engineering design of muscular structure-function relationships in an automated fashion.

INTRODUCTION

For marine life forms, both biomechanical and hydrodynamic forces place physical constraints on swimming speeds, promoting the convergent evolution of swimming strategies and fin shapes. Given that these constraints are scale dependent, such as the Reynolds number (*Re*), this results in natural locomotive scaling laws that govern how fast an organism can swim on the basis of its size and body kinematics (*1*, *2*), with larger organisms generally swimming faster than smaller ones. Within this context, biohybrid swimmers have recently emerged as a distinct class of soft robots that integrate living tissue with synthetic components to create self-powered muscle-based microrobots (*3*). Similar to classic robotics, biohybrids can actuate, allowing them to walk, crawl, and swim, along with forming more complex behaviors such as pumping and gripping (*4*). As a result, these devices have garnered interest for use in remote sensing, in studying muscle regeneration and development, and as medical robots for drug delivery (*3*, *5*–*8*). However, in building biohybrid swimmers, researchers primarily use a "biomimetic" approach, which attempts to recreate preexisting biological structures (*9*–*11*). Using this strategy for fin design may be limiting, because many of the proposed applications for biohybrids require them to swim at different length scales than their naturally occurring inspirations. This makes it challenging to determine which fin structures to mimic, given that marine life-forms can display a wide range of morphologies depending on their local swimming environment (*12*, *13*). In addition, ignoring scale-dependent physical constraints in the design of biorobotic systems can result in limited swimming speeds relative to similarly sized biological organisms (*2*, *14*, *15*). The inability of these devices to match natural scaling laws points toward the inefficient use of muscle mass, suggesting the need for improved methods of design. This motivates the following question: How do we select fin geometries to operate under previously untested working environments that also preserve natural scaling laws in terms of swimming speed and efficiency?

Recent advances in machine learning, including the use of neural networks (NNs), may offer a potential solution for designing efficient fin geometries. Applying the engineering design algorithm (design-build-test-learn) in a programmatic fashion allows for automated design, such as for jumping and crawling robots (*11*, *16*, *17*), as well as biorobotic systems (*18*, *19*). However, when it comes to soft-robotic swimming devices, this iterative approach can be challenging. Although computational fluid dynamics (CFD) may be used to model the behavior of individual fin geometries (*20*–*22*), swimming is a multiphysics problem, requiring computationally intensive kinematic and fluid-dynamic modeling. As a result, researchers have attempted to minimize the number of simulations performed by carefully selecting which configurations to simulate in each iteration. Previous methods for addressing this challenge have included statistically driven approaches such as Bayesian optimization (*23*–*25*); however, recently, modern machine learning algorithms have made this class of design problems tractable (*26*). In particular, NN-directed approaches, which make use of deep learning models to suggest potential design configurations, can help accelerate this process and have been used in applications such as material synthesis (*26*–*30*) and de novo protein design (*31*–*33*). This suggests that a similar approach may be applied to biohybrid fin design, helping improve device performance by more efficiently searching within a defined parameter space.

Inspired by naturally occurring batoids, such as skates and rays, here, we used soft-robotic biohybrid rays combined with machine learning to optimize ray fin geometries for fast swimming at millimeter-length scales (Movie 1). We hypothesized that by using a machine learning–directed optimization (ML-DO) approach, we could more efficiently search for fin designs that maximize their relative swimming speed. To test this, first, we developed a genetic algorithm for expressing a multitude of different fin geometries that can be realized using biohybrid systems; second, we described a generalized ML-DO

[1]Disease Biophysics Group, John A. Paulson School of Engineering and Applied Science, Harvard University, Boston, MA 02134, USA. [2]Medical and Health Informatics Laboratory, NTT Research Inc., Sunnyvale, CA 94085, USA.
*Corresponding author. Email: kkparker@seas.harvard.edu
†Present address: Department of Statistics, Texas A&M University, College Station, TX 77843, USA.
‡Present address: Department of Chemical and Biomolecular Engineering, Samueli School of Engineering, University of California, Irvine, CA 92697, USA.

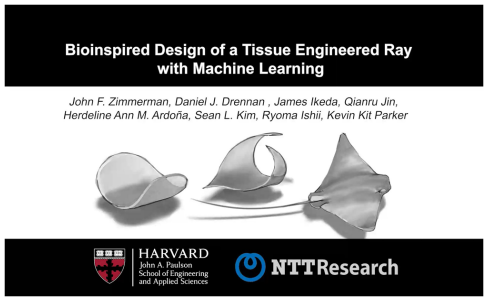

Movie 1. Machine learning for studying biohybrid structure-function relationships. Summary movie describing a machine learning–directed optimization approach for designing biohybrid minirays.

approach for searching within a large discontinuous configuration space; and third, we used this methodology to identify biohybrid fin geometries for high-performance swimming at low *Re* values. Using machine learning, we were able to quantitatively explore fin structure-function relationships, reconstructing general trends in pelagic batoid morphology. This showed how fins with large aspect ratios (ARs) and fine tapered tips preserved their utility across multiple length scales in mobuliform swimming. Following these designs, we then built biohybrid minirays out of engineered cardiac muscle tissue, which were capable of self-propelled swimming at the millimeter-length scale and demonstrated improved swimming efficiencies in terms of natural locomotive scaling laws as compared with previous biomimetic designs. Overall, this work shows how an iterative bioinspired design approach can be used to quantify form-function relationships while predicting the emergence of natural fin geometries from basic physical constraints.

RESULTS

Generating ray fin geometries

Acting as a planar muscular pump, the pectoral fin geometry of skates and rays depends strongly on their local habitat (*12*, *13*). Slow rajiform swimmers, such as the Atlantic ray (*Dasyatis sabina*), have small ARs and rounded fin morphologies (*34*). Conversely, fast mobuliform swimmers, such as the cownose ray (*Rhinoptera bonasus*), have triangular fins with larger ARs and sharp tapering tips (Fig. 1, A to C) (*35*, *36*) . To recreate this diverse range of pectoral fin morphologies, we developed a genetic algorithm. Inspired by proteins, where a limited set of amino acids can be interchanged to form a multitude of structures, we used Bézier curves as geometric basis functions, which could be combined or swapped to form distinct fin shapes (Eqs. 1 to 3 and fig. S1, A and B). In total, 14 basis functions were selected, with each being assigned a representative letter (A to N). These included the set of simple perturbations of two Bézier control points (P_1 and P_2) (fig. S1C), with two basis functions encoding for changes in AR (A and N) and an additional four basis functions for intermediate curvature (D, E, J, and K). These bases could be linearly combined in a weighted sequence to form a distinct identifier or a spline-derived naming assignment (sDNA) that uniquely described each ray's geometry. This enabled a diverse range of fin geometries, with smooth transitions between neighboring sequences (fig. S1, D to F). Using sDNA sequences, we were then able to recreate multiple existing batoid fin morphologies (fig. S2), with an increasing number of basis functions allowing for a more precise fit [coefficient of determination (R^2) = 0.906 and 0.996 for a 3- and 12-basis representation of *D. sabina*, respectively]. Restricting our design space to combinations of six basis functions allowed for a reasonable approximation ($R^2 > 0.95$ in each case; fig. S2) of existing batoid morphologies while still enabling a wide variety of possible configurations (>7.5 million).

Biohybrid ray fabrication

Having developed a method for generating distinct fin shapes, we reasoned that this approach could be used to explore form-function relationships in fin design. To build free-floating biohybrid minirays, we modeled our approach after muscular thin films (MTFs) (*37*, *38*), where we fabricated thin film segments using a neutrally buoyant polydimethylsiloxane (PDMS) blend that could be cut into distinct fin geometries defined by an sDNA sequence (fig. S3). Fins were then positioned about a thicker central column that served as a "spine" (fig. S4). This restricted anterior-posterior bending, preventing the formation of tubular structures (fig. S5). For locomotion, samples were microcontact printed with fibronectin (FN) line patterns and seeded with cardiomyocytes [neonatal rat ventricular myocytes (NRVMs)]. Fibronectin provided geometric cues that could potentiate cardiomyocyte alignment, forming laminar anisotropic myocardium capable of spontaneous and paced contraction (Fig. 1D, i and fig. S6) (*2*, *37*, *39*). By linearly scaling geometries, the surface area was conserved across each design, resulting in a consistent muscle mass. Upon release, this resulted in free-floating biohybrid ray models (Fig. 1D, ii and Movie 2), which were planar during diastole and transitioned to ventral deformations during systole (fig. S3F and movie S1).

For rays to achieve self-propulsion, a nonsymmetric stroke pattern is required. Cownose rays accomplish this by changing their fin's angle of attack throughout their stroke (Fig. 2A). To recreate this pattern, we introduced an acute patterning angle ($\alpha = 30°$) between the longitudinal axis of the cardiomyocytes and long axis of the fins (perpendicular to the central column) (Fig. 2B). This resulted in an undulatory motion that was reminiscent of the cownose ray, showing minimal deflection below the ventral axis (*13*) while exhibiting a similar stroke hysteresis (Fig. 2, C to E, and movie S2). To determine whether this motion could propel fluid, we then submerged the fins in a bath containing fluorescently labeled beads using particle imaging velocimetry (PIV) to reconstruct the surrounding fluid-velocity field. Here, we observed vortex formation along the lateral free edges of the fin (Fig. 2, F and G), similar to those produced by marine life-forms (*40*). Quantifying the thrust generated by these films, we found that angled fin geometries ($\alpha = 30°$) were able to produce greater positive net thrust than perpendicular aligned tissues ($\alpha = 0°$) (fig. S7). Incorporating these angled structures into the biohybrid fin design resulted in free-floating rays that displayed autonomous shape-dependent locomotion (fig. S8 and movie S3), with the relative thrust and swimming velocity depending on the fin geometry (fig. S9, eq. S1, and movie S4). By conserving the fin's surface area and total muscle mass, this offered an approach for determining the relative thrust provided by each fin shape while showing that angled fins could be used to generate self-propulsion in biohybrid rays.

Kinematics and CFD

To model biohybrid mechanics, fins were simulated using a kinematic model of thin-film deflection coupled with the lattice-Boltzmann

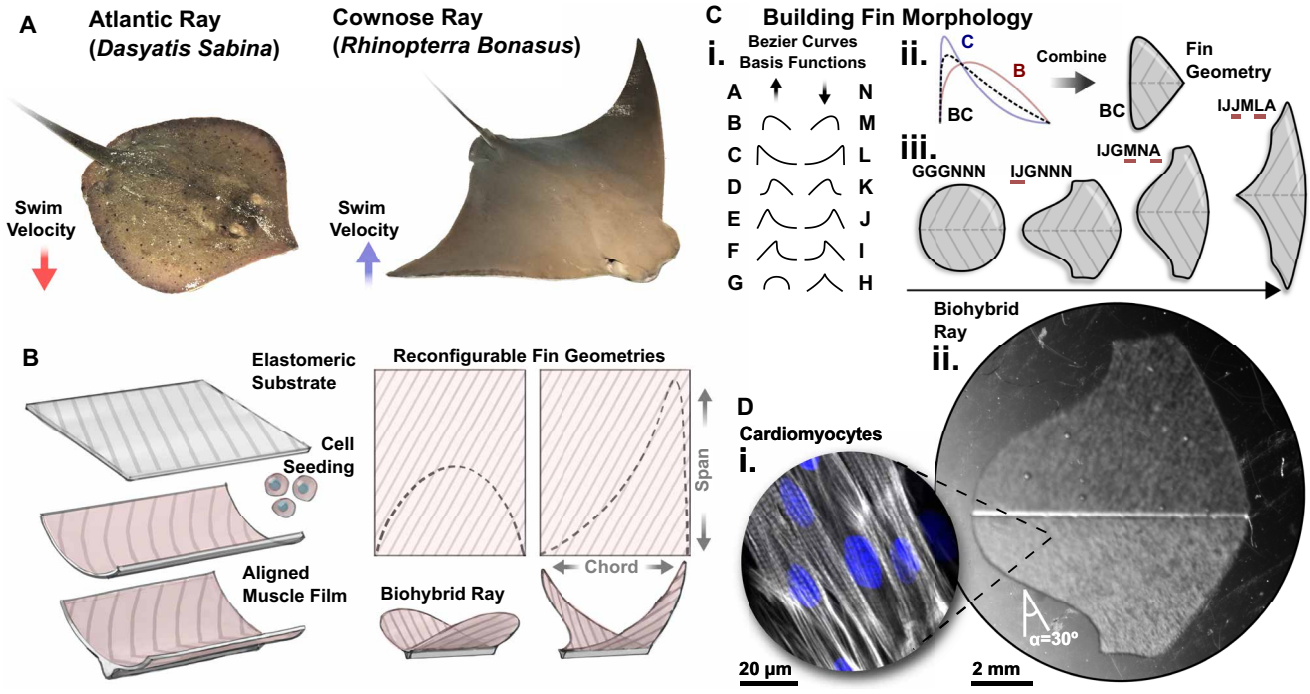

Fig. 1. Reconfigurable biohybrid fin design. (**A**) Photographs of an Atlantic ray (*D. sabina*) and a cownose ray (*R. bonasus*) showing distinct pectoral fin geometries. (**B**) Schematic depicting the design of biohybrid rays, where segments are taken from aligned muscle films to form reconfigurable pectoral geometries. (**C**) Genetic algorithm for defining fin morphology. (i) Geometric basis functions made up of Bézier curves are (ii) combined in sequence to form closed-form shapes. (iii) Changes in sequence combinations (underlined in red) can be introduced to allow for smooth transition between similar geometries. (**D**) Shapes produced using the genetic algorithm can be realized as free-floating biohybrid rays, showing a high-magnification immunofluorescent stain (i) of aligned cardiomyocytes [sarcomeric α-actinin (gray), nucleus (blue); scale bar, 20 μm], with corresponding low-magnification dark-field image (ii). Scale bar, 2 mm.

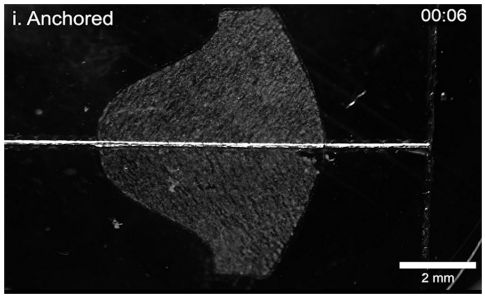

Movie 2. Biohybrid ray manufacture. (**i**) Top-down view, depicting a biohybrid ray fabricated using NRVMs, which has been anchored to the underlying substrate via its spine (1-Hz field stimulation). (**ii**) High-magnification view of aligned NRVM tissues on the fin surface, spontaneously contracting. (**iii**) Free-floating biohybrid ray after being released from the underlying substrate, showing autonomous locomotion (1-Hz field stimulation).

method (LBM) for CFD (Fig. 2, E to G). Kinematics were approximated (fig. S10) following Stoney's equation for thin-film deflection (eq. S2) (*41*). Hysteresis was incorporated by assuming that the film's position could be represented as a linear combination of the anisotropic stress of muscle contraction and the isotropic restorative force of the underlying elastomeric substrate (eqs. S3 to S5). This resulted in a model of fin kinematics that recapitulated experimental observations, such as the apparent time- and angle-dependent fin deflection and stroke hysteresis (fig. S11 and movie S5A) and could be used to calculate the time-dependent surface velocity profiles of arbitrary fin geometries (Fig. 2E). Surface velocities were then coupled in a one-way manner to fluid dynamics simulations.

Fluid dynamics simulations were performed using the LBM, which numerically approximates fluid collisions and relaxation, implicitly solving the Navier-Stokes equations (*42*–*44*). Fin dynamics were simulated in a flow chamber using a three-dimensional (3D; D3Q15) LBM model (eqs. S6 to S15 and fig. S12), assuming periodic boundary conditions for the inlet and outlet and Dirichlet boundary conditions for the remaining sidewalls (*45*). This application of the LBM was tested using common CFD benchmarks, such as a lid-driven cavity and an occluded pipe, which displayed eddy current formations and rerouted laminar flows, respectively (fig. S12, A and B, and movie S6) (*44*). For biohybrid rays, a low-*Re* regime was assumed ($Re = 60$) on the basis of PIV measurements taken for initial fin geometries. In the simulation, momentum was then transferred from the fins using a no-slip moving obstacle boundary condition (eq. S13 and fig. S11D) (*46*). In addition, to account for time discretization artifacts, fluid flows were simulated at 10× the rate of the film kinematics (600 and 60 Hz, respectively). This resulted in fluid-velocity fields that resembled those observed experimentally, both in their vortex formation and direction of flow (Fig. 2G and movie S5B). Acting as a forward model for simulating differences in fin design, we then examined how features such as tissue alignment affected swimmer performance, with angled geometries ($\alpha = 16°$ to $30°$) providing the most thrust (fig. S13). In addition, this could be used to model how changes in fin geometries (Fig. 2H) were predicted to influence miniray performance.

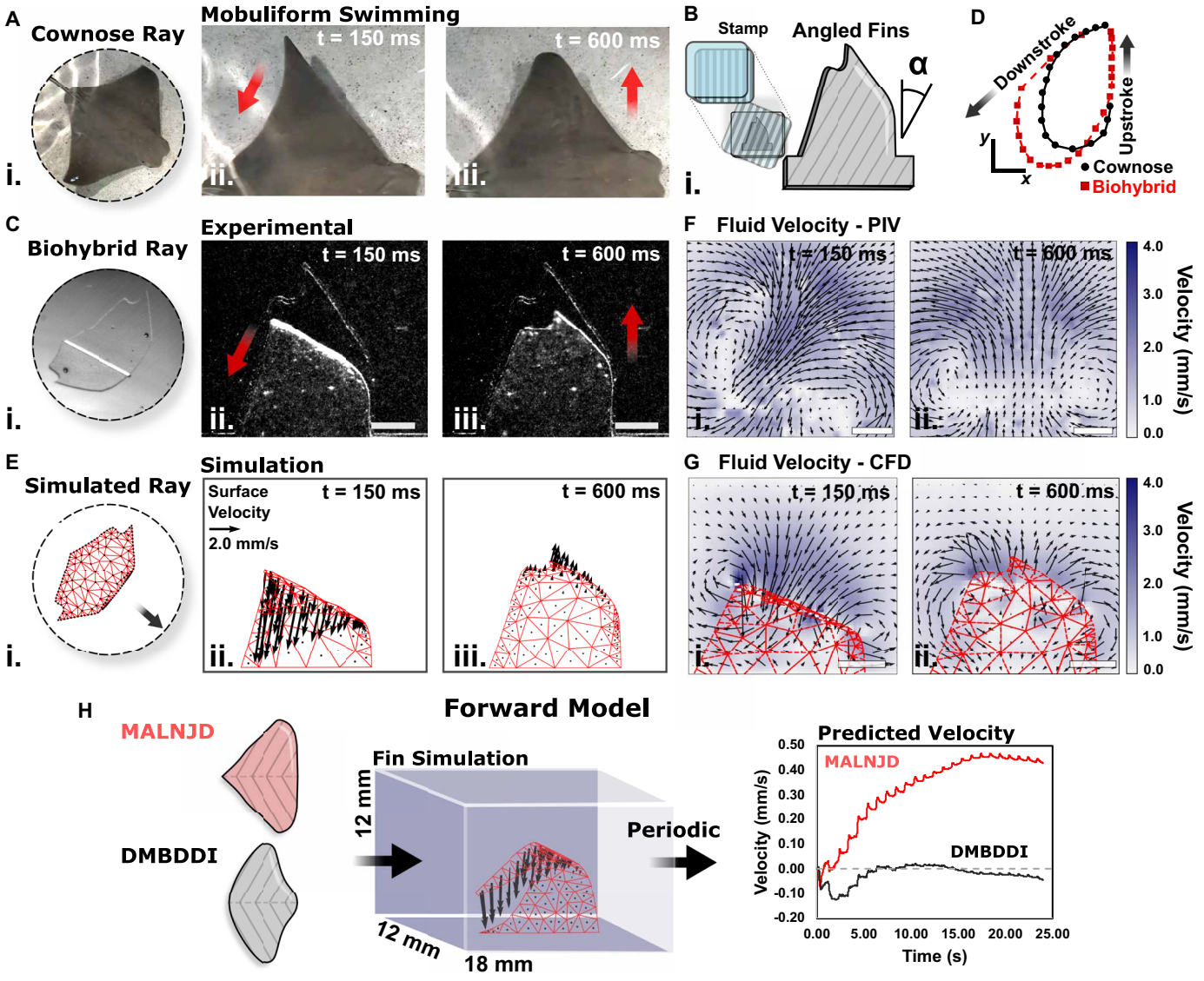

Fig. 2. Forward modeling of mobuliform swimming. (**A**) Photograph of a cownose ray (*R. bonasus*) (i) with corresponding time lapse of fin deflection (ii and iii) during mobuliform swimming (specimen ~35 cm in length, not including tail). (**B**) Schematic showing the fabrication of angled biohybrid fin geometries. (**C**) Dark-field micrograph of biohybrid film deflection during systole (ii) and diastole (iii) ($\alpha = 30°$; sDNA: EIDLML) Scale bar, 1 mm. (**D**) Path of travel for the tip of the fin of a cownose ray (black) and a biohybrid ray (red) as normalized by fin length (FL), indicating a hysteresis in the stroke pattern, with the biohybrid rays recapitulating mobuliform swimming. Scale bars, 0.1 FL. (**E**) Corresponding kinematic simulation of the fin dynamics, using a Delaunay mesh reconstruction (black arrows indicate surface velocity of each mesh). (**F**) Experimental and (**G**) CFD-simulated measurements of the fluid-velocity field surrounding the example fin geometry during systole (i) and diastole (ii). Scale bars, 1 mm. (**H**) Schematic of the fluid dynamics simulation domain, providing a forward model for going from fin geometry to predicted swimming velocity (velocity profiles given for two example geometries).

Machine learning–directed optimization

Using the LBM as a CFD simulation method, we then sought an approach for selecting which fin geometries to simulate. The size of the parameter space makes it difficult to span directly using traditional computational approaches (~200 years of direct compute time). Hence, we required a more efficient method for searching. Here, we reasoned that using an ML-DO approach (Fig. 3A, Movie 3, and fig. S14) may provide an efficient method for mapping the performance of fin geometries. In ML-DO, an NN is iteratively trained to make increasingly accurate predictions about ray performance on the basis of their fin geometry. In this approach, selected fins are first simulated using CFD, with their relative performance acting as a training set to inform an NN model. The NN then predicts which remaining geometries are likely to have the greatest velocities, and this information is used to select the next generation of fin shapes. Given the ability of NNs of sufficient complexity to serve as universal function approximators (*47*, *48*), we reasoned that this approach would allow the network to iteratively refine its understanding of how fin shape contributes to swimming while progressively forming a more accurate representation of the underlying target function.

Testing ML-DO, we performed benchmarks on a contrived multimodal hyperbolic trial function, where the best inputs are known a

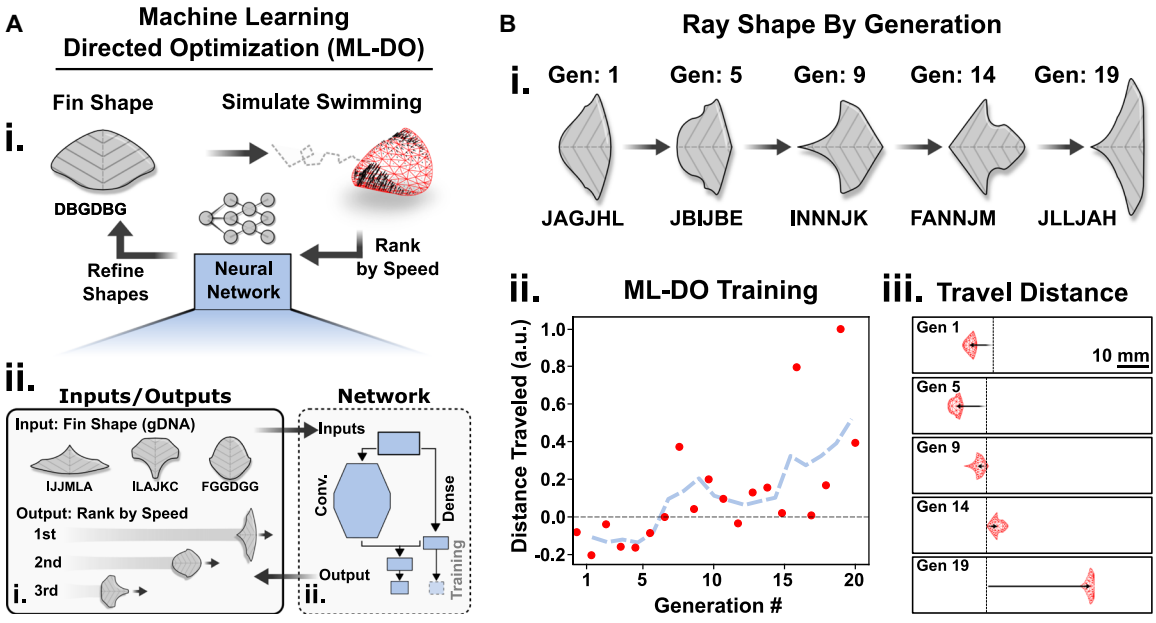

Fig. 3. ML-DO of fin morphologies. (**A**) (i) Schematic of the ML-DO process as applied to selecting fin morphologies (ii), with the corresponding network architecture, model inputs (sDNA), and outputs (rank). (**B**) Results of the ML-DO process for selecting biohybrid fin geometries. (i) Fastest fin geometry for a given generation as predicted by ML-DO. (ii) Average normalized distance traveled for the central hypothesis of each generation (red dots) as predicted by the NN, with a moving average (blue line). (iii) Corresponding top-down view of the ray's simulated travel distance.

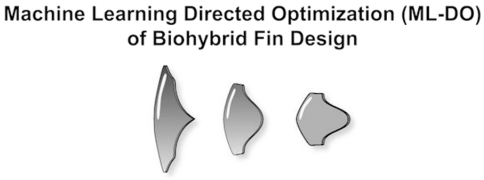

Movie 3. ML-DO flow chart. Video depicting the ML-DO process for iteratively improving ray performance on the basis of fin geometries. (**i**) First, a batch of sDNA sequences are simulated using kinematic and CFD modelling to predict swimmer travel distance. (**ii**) Swimmer performance data are then prepared for machine learning, turning travel distances into a speed ranking label using a Gumbel distribution. (**iii**) An NN is trained on the existing swimmer data, making predictions about which geometries are likely to result in the fastest swimming. (**iv**) On the basis of the trained NN model, new sDNA sequences are selected for the next round of simulation. Collectively, this forms an iterative model for predicting fast swimming fin geometries.

priori (fig. S15). Using this trial function, we then examined different NN architectures and sampling strategies. Among the NN architectures considered (fig. S15A), we found that a mixed network architecture, combining fully connected and convolutional layers, displayed the most efficient learning (fig. S15B), identifying the greatest number of high-ranked targets (defined as the top 2000 configurations) given a limited set of training examples (see Supplementary Methods for details). Using the same metric to quantify sampling methods, we found that a clustered-directed evolution (cDE) showed the most efficient learning among the strategies surveyed, especially compared with random sampling methods (fig. S15, C to E). Combining these strategies, we then compared ML-DO with other leading high-performance derivative-free optimization algorithms, including covariance matrix adaptation–evolutionary strategies (CMA-ESs) (*23*, *24*), DE (*32*, *49*), and Bayesian optimization (BayesOpt) (*25*). In this numerical trial, we found that ML-DO was able to recognize the greatest number of known high-ranked sequences (fig. S16), identifying on average 80 ± 7 after only sampling 850 training examples. This contrasts with CMA-ES, which correctly predicted only 0.4 ± 0.2, on average, with most trials failing to find even a single high-ranked sequence (fig. S17). Using the same starting information, DE and BayesOpt correctly predicted only 37 ± 3 and 57 ± 5 sequences on average, respectively (figs. S18 and S19). This ~40% improvement over other leading methods indicates that ML-DO may provide substantial advantages when exploring discrete input spaces with a limited amount of training data.

Next, simulating different fin shapes, we implemented ML-DO as an iterative design tool for selecting high-performance biohybrid fin geometries. Although the fitness of real marine life forms is determined by their ability to reproduce and form offspring, we reasoned that for many such organisms, the ability to swim quickly is critical to this endeavor, given that it allows them to gather food and avoid predation. Therefore, as an objective function for ray performance, we chose the total distance traveled by each miniray during a fixed duration (in the forward direction). To improve model training, swimming velocities were then normalized into percentiles ranked by speed (between 0 and 1), approximating empirical quantiles for each ray's performance according to a Gumbel measure (*50*). This resulted in an ML-DO model that showed iterative improvements in miniray performance (Fig. 3B), with subsequent generations displaying increased travel distances (Fig. 3B, iii). For the final ranking of rays, simulations were split into training and test datasets (~1000:150), with the NN providing a mean square error (MSE) of 6.8% (CDF range: 0 to 100%) or a root mean square error (RMSE) of 26%. These data suggest that the NN was able to effectively rank fin geometries on the basis of their swimming velocity and could potentially be used to extract trends in ray performance.

Structure-function relationships in biohybrid fin morphology

Naturally occurring pelagic batoids are characterized by fins with large ARs, sharp tips, and tapered trailing edges, which lead to increased thrust, reduced drag coefficients, and smooth acceleration (*34*, *51*). To see whether these features were preserved for mobuliform swimming at the millimeter scale, we then examined how the NN determined the contribution of different fin morphologies to ray performance. This was achieved by measuring the average predicted change in a fin's speed ranking on the basis of the normalized contribution of each basis function (eq. S16), for both randomly selected (fig. S20) and top predicted rays (Fig. 4A). Here, we observed that basis functions that presented sharper tips were favored over smoother basis functions, such as E over B and J over M. Similarly, basis functions that contributed to an anterior center of mass—such as J, K, and L—were highly favored over posterior basis functions, including B, C, and D. In contrast, basis functions that contributed to increased ARs, such as A to N and G to H, were modestly disfavored for average rays (fig. S20A) but were highly selected for in the top performers (Fig. 4A). This suggested that larger ARs may contribute to increased thrust generation, leading to either highly positive or highly negative travel rates (in the reverse direction) when coupled to anterior or posterior centers of mass, respectively.

To quantify these effects, we then evaluated how the swimming rate was expected to differ as a function of mass distribution and ARs (Fig. 4B). In both the average and top performance cases, ML-DO favored anterior centers of mass (relative to tissue angle, α). Although not observed in nature, this behavior is reasonable for current biohybrid models because of restricted kinematics arising from the fixed tissue angle, α, and the resulting pinned region (fig. S10G) (*38*). With the anterior-posterior axis being defined by the angle of the muscle tissue, posterior distributions result in larger pinned regions and, therefore, lower contributing muscle mass. Because swimmers with posterior distributions will swim in the "reverse" direction, this limits their overall speed relative to anterior mass distribution (fig. S21). Testing this experimentally in biohybrid rays with a mirrored anterior-posterior axis (on the basis of the tissue angle, α), we found that fins with a primarily posterior mass distribution tended to be stationary, in contrast with anterior distributions, which resulted in increased mobility as predicted (movie S7). ML-DO also predicted that the AR plays an important role in regulating ray locomotion, with larger wingspans leading to increased propulsion (Fig. 4B). This was broadly consistent with phylogenetic trends

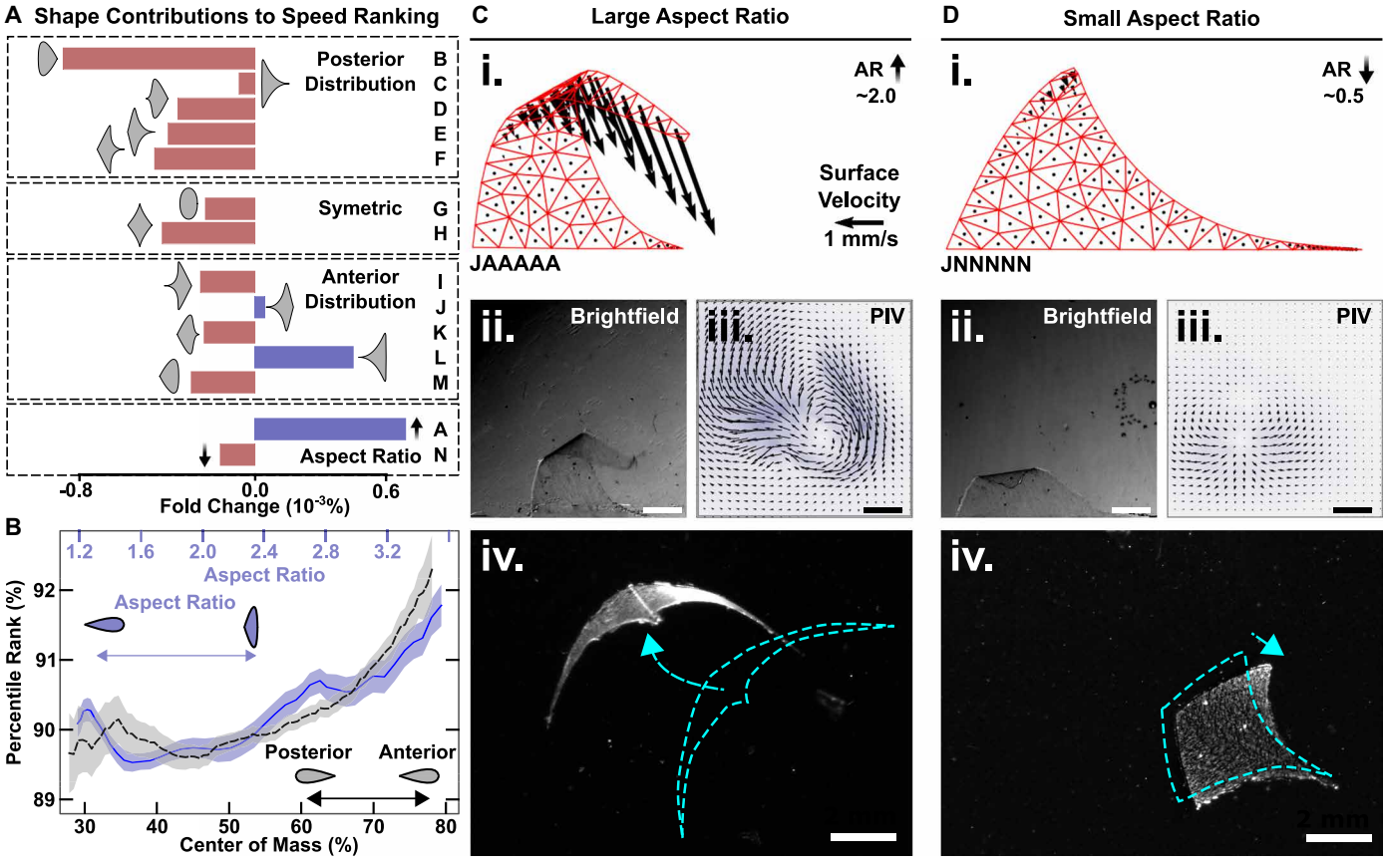

Fig 4. Extracting trends in ray performance. (**A**) (i) Contribution of each basis function to swimmer performance as predicted by the NN (red, negative contribution; blue, positive contribution; given as the average fold change in ranking relative to the top 20,000 predicted rays). (**B**) Ray's projected performance based on the AR; the AR (blue, top axis; wing span:body length) and mass distribution (gray, bottom axis) (given as the average percentile rank based on the top 20,000 predicted rays; shaded regions indicate SEM). (**C** and **D**) (i) Surface velocity profiles for rays with large [(C), JAAAAA AR: ~2.0] and small [(D), JNNNNN AR: ~0.5] ARs, showing that large ARs lead to increased velocities (arrow key indicates 1 mm/s). (ii) Accompanying bright-field micrograph and fluid velocity profile (iii) of the surrounding fluid, taken during systole. Scale bars, 1 mm. (iv) Dark-field micrograph of biohybrid rays after 12 s, indicating that large ARs lead to increased travel distances (teal outline indicates initial position at $t = 0$ s, time-averaged background subtracted and contrast adjusted). Scale bars, 2 mm.

in naturally occurring mobuliform batoids (*35*, *52*), suggesting that this trait is preserved across length scales. Studying this further, rays sharing the same morphology but differing ARs were both simulated and physically fabricated (Fig. 4, C and D, i and ii and movie S8). Large ARs were linked with increased surface velocities near the tip of the fin, larger vortex formation, and greater total locomotion (Fig. 4, C and D, iii and iv and fig. S22). This is likely the result of longer muscular fibers contributing to a greater average moment arm across the surface of the fin and, therefore, a larger biomechanical advantage. Collectively, this demonstrated that both the AR and centroid location play an important role in regulating swimming speeds for biohybrid rays, suggesting that the AR in particular serves as a key metric for defining performance in mobuliform swimming regardless of the length scale.

Maximizing swimming velocity

Applying these findings, we then sought to identify which sDNA sequences provided the greatest total swimming speeds. Using ML-DO to iteratively maximize ray swimming velocity resulted in an approximate mapping of the functional landscape (Fig. 5A and movie S9) relating fin shape to swimming velocity. Here, ML-DO identified the sDNA sequences JLLJAH, LEJMHN, and FCBHFA as having the greatest, middle, and lowest speed rankings, respectively. This indicated that rays with large ARs and sharp tips represented both the top and bottom performers, being predominately reversed along the anterior-posterior axis (defined by the tissue angle, α), with bottom performers being expected to travel in the posterior direction. Meanwhile, a wider body plan was predicted for the middle performance ranges. Testing these predictions, biohybrid rays were fabricated (Fig. 5B, ii), and their relative rates of travel were compared (Movie 4 and movie S10). Velocities were normalized on a per-stroke basis, accounting for out-of-plane locomotion (fig. S23). This yielded relative velocities that were consistent with the ML-DO model (Fig. 5, C and D), with a maximum absolute velocity of ~1.1 mm/s for JLLJAH (fig. S24). Overall, this indicated that ML-DO was able to accurately predict which fin geometries would display the greatest rates of travel in biohybrid minirays, selecting JLLJAH as the highest performance configuration.

Natural locomotive scaling laws

We then sought to understand how JLLJAH performed relative to previous biomimetic designs and naturally occurring swimmers.

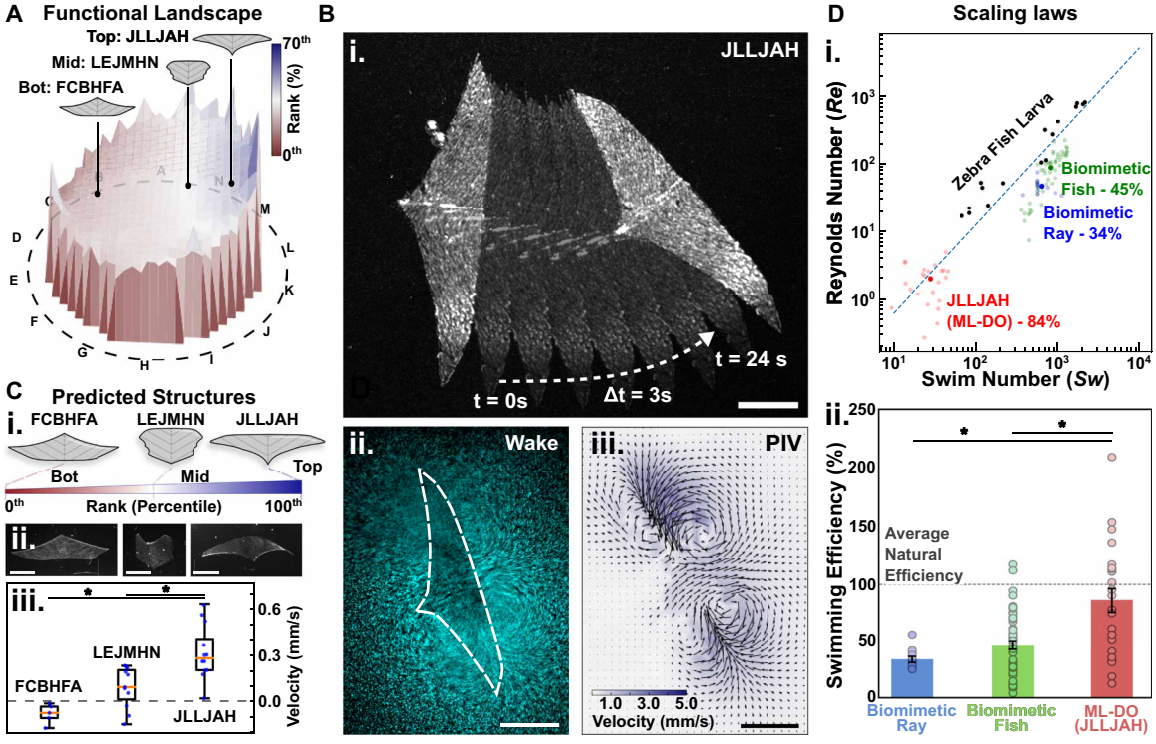

Fig. 5. Building biohybrid rays to follow natural scaling laws. (**A**) Radar plot projection of the functional landscape of ray performance as predicted by the NN, relating fin shape to swimming speed (based on $n > 1000$ simulations) (projection from 14D space, with the letter axes indicating the direction of a given sDNA basis function). (**B**) Composite projection of top performing ray geometry (JLLJAH) overtime showing forward travel (i) (increased contrast given to $t = 0$ and 24 s). Fluorescent beads showing the wake generated during swimming (ii) (maximum projection over 8 s), with corresponding fluid velocity fields showing vortex generation (iii). All scale bars, 2 mm. (**C**) Top (JLLJAH), middle (LEJMHN), and bottom (FCBHFA) performing ray configurations (i), as predicted by ML-DO after training. (ii) Dark-field micrograph of corresponding biohybrid ray configurations, released and swimming. Scale bars, 2.5 mm. (iii) Box plot of normalized ensemble swimming velocity of biohybrid ray models, corresponding well to ML-DO–predicted trends in performance (JLLJAH, $n = 12$; LEJMHN, $n = 11$; and FCBHFA, $n = 5$, with n representing separate tissue-engineered rays, boxplot given in quartiles). (**D**) (i) Scaling analysis between wild-type and paced biohybrid swimmers (individual measurements given as transparent dots, with larger opaque dots indicating average performance). (ii) Swimming efficiency of biohybrid rays relative to natural locomotive scaling laws ($n = 23$ ML-DO, $n = 13$ biomimetic rays, and $n = 54$ biomimetic fish) (error bars = SEM). Data for biomimetic rays and fish taken from (*2*) and (*15*), respectively. $^*P < 0.05$.

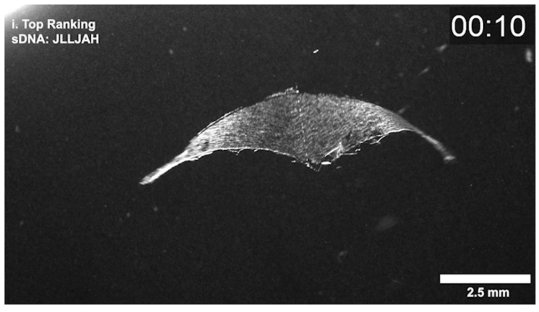

Movie 4. Comparison of ML-DO–predicted geometries. Example of biohybrid rays swimming for ML-DO–predicted fin configurations. Includes the geometry predicted to travel the farthest (**i**) (CDF = 1.0, JLLJAH), the least (**ii**) (CDF = 0.5, LEJMHN), and the most likely to travel in the posterior direction (**iii**) (CDF = 0.0, FCBFHA).

Current biohybrids operate under laminar flows ($Re < 10^2$), in contrast with natural batoids, which swim in a turbulent regime ($Re > 10^4$ to 10^6) (*21*). This makes it difficult to form a direct comparison. In nature, however, marine life forms follow natural locomotive scaling laws that relate their body size and kinematics to their swimming speed (*1*, *2*). In the laminar regime, these scaling laws are given by $Re \sim Sw^{4/3}$, which is defined as follows

$$Re = UL/\nu \tag{1}$$

where U is the swimming velocity, L is the characteristic fin length, ν is the fluid viscosity, and Sw is the dimensionless swimming number, given by

$$Sw = \omega AL/\nu \tag{2}$$

such that ω and A are the frequency and amplitude of fin undulation, respectively. Relating these two factors then provides a convenient benchmark for understanding how efficiently a fin's shape, and therefore muscle mass, contributes to its locomotion at different length scales. Here, the expected natural swimming efficiency, S_{EF}, is given by

$$S_{EF} = \frac{Re}{\kappa Sw^{4/3}} \tag{3}$$

where κ is an empirically determined proportional constant ($\kappa = 0.03$), found by fitting these scaling laws to extant biological data (*1*). Although this does not represent a thermodynamic limit (individual larvae from the same species, for instance, displayed between 70 and 340% swimming efficiencies), biohybrids that match this benchmark would be following average trends in natural swimming performance, with those falling below this standard representing an inefficient use of muscle mass. Here, we found that ML-DO–generated miniray fin geometries were, on average, 85 ± 10% (mean ± SEM) as efficient as those of naturally occurring swimmers (Fig. 5D, i). This contrasts with previous biomimetic designs, which were point stimulated and used scaled versions of naturally occurring fin geometries with varying swim strategies. This included biomimetic rays (rajiform swimming), which were only 34 ± 2% efficient as natural rays (*2*), and biomimetic fish (body-caudal fin swimming), which were 46 ± 4% as efficient (*15*) (Fig. 5D, ii). This indicates that a machine learning–based approach can yield improved device performances relative to the direct translation of macroscopic fin geometries. In addition, because the ML-DO–generated rays begin to approach natural scaling efficiencies, this suggests that they may potentially be used as a model system to help us better understand how fin geometry contributes to swimming performance.

DISCUSSION

Using an ML-DO approach, we were able to identify high-performance fin geometries, fabricating biohybrid rays that were able to propel themselves using mobuliform swimming at the millimeter-length scale, showing that both their velocity and swim direction were dependent on their fin geometry. Although the devices presented here demonstrated greater efficiency (~2×) than other recent biomimetic designs (*2*, *15*), they were still slightly less efficient, on average, than naturally occurring marine life forms (*21*). This could be the result of several factors. First, in this work, muscle designs were limited to a single linear anisotropic tissue layer, in contrast with the musculature of natural batoids, which is curvilinear and occurs in a laminar architecture across multiple layers (*53*). Although some of these features could be recapitulated with more advanced patterning, scaling this into three dimensions is difficult both in terms of kinematic modeling and device fabrication. Second, because the structural optimization is only as good as the numerical modeling, the current fluid dynamics simulation model did not account for rotational displacement (pitch, yaw, and roll). Given that the relative position of the center of mass and thrust are important for controlling stability in mobuliform swimming (*54*), this resulted in some out-of-plane locomotion for physical rays when far from a barrier, which limited their overall forward propulsion. Third, the current study was limited to 20 generations; however, swimming speed was still on an upward trajectory during training. This suggests that additional rounds could help further refine device performance, resulting in higher maximum velocities. Although additional work is needed to completely match natural scaling laws, this study helps demonstrate an initial approach for moving past direct biological replication and forming rationally engineered biohybrid swimming devices for operation in previously untested working environments.

Aside from selecting efficient biohybrid fin geometries, ML-DO may also provide insights into the selective pressures guiding fin morphogenesis. In nature, marine life forms have undergone a cost-benefit analysis via natural selection to produce their current fin morphologies (*9*). Although natural selection comprises many different factors, regarding fin geometry, this selection process is bound by consistent physical constraints such as fluid viscosity, muscular contractility, and moment arm generation. These constraints impose performance limits as defined by the system's hydrodynamic properties, which results in convergent gaits (*1*). In ML-DO, we are searching within a similar set of physical constraints to help establish structure-function relationships for biohybrid fin designs. Therefore, it follows that ML-DO would converge on fin shapes that share features in common with naturally occurring rays because these structural motifs help solve a similar set of biomechanical constraints, albeit at different length scales. Although morphological features such as large ARs and fine pointed tips have previously been identified as playing an important role in regulating batoid evolution (*34*, *51*), directly quantifying how these features map to swimming speed has been difficult. When adjusted for macroscopic length scales, ML-DO may be able achieve this, providing further insight into the evolution of ray fins.

In addition to biohybrid fin design, ML-DO may also serve an important role in studying broader structure-function relationships within biology. Given the flexibility of NNs to adopt diverse inputs and objective functions, this approach could be readily extended to study other more morphologically complex muscular pumps, such as the heart. ML-DO's ability to map functional landscapes in an automated fashion could provide valuable insights into the selective

pressures guiding ventricle shape, alignment, and loop formation (*55*–*58*). In addition, given recent advances in the additive manufacturing of cardiac structures (*59*–*61*), the structural predictions made using ML-DO could be tested using tissue-engineered constructs, in a similar manner to the biohybrid rays demonstrated here. Overall, this suggests that, going forward, using an iterative bioinspired design approach may help us better understand form-function relationships in both robotics and naturally occurring systems.

MATERIALS AND METHODS

NRVM culture

Rat ventricular cardiomyocyte isolations were performed following standard protocols as previously reported (*37*, *38*) and as approved by Harvard University's Institutional Animal Care and Use Committee, which adhere to the National Institutes of Health (NIH) Guide for the Care and Use of Laboratory Animals. The hearts of 2-day-old neonatal Sprague-Dawley rat pups, both male and female (Charles River Laboratories, Wilmington, MA), were surgically removed following approved humane euthanasia procedures, and ventricular tissue sections were isolated. These were partitioned into six to eight approximately equal segments using surgical scissors while submerged in Hank's balanced salt solution (HBSS) (Thermo Fisher Scientific, Waltham, MA). Tissue sections were then rinsed in fresh HBSS before being digested overnight (13 to 14 hours) in a cold (4°C) trypsin solution (1 mg/ml in HBSS) (MilliporeSigma, St. Louis, MO), under gentle agitation using a rocking plate. After this initial digestion, samples were further dissociated using four repeated rinses of collagenase solution (1 mg/ml in HBSS) (MilliporeSigma, St. Louis, MO) at 37°C. The resulting cells were then concentrated using centrifugation (4 min at 200*g*) and resuspended in M199 medium (Life Technologies, Carlsbad, CA) containing 10% (v/v) heat-inactivated fetal bovine serum (FBS; Life Technologies, Carlsbad, CA), vitamin B12 (2 mg/liter), 10 mM Hepes (Life Technologies, Carlsbad, CA), penicillin (50 U/ml; Life Technologies, Carlsbad, CA), 2 mM L-glutamine (Life Technologies, Carlsbad, CA), glucose (3.5 g/liter; MilliporeSigma, St. Louis, MO), and 1% minimal essential medium with nonessential amino acids (Life Technologies, Carlsbad, CA). The resulting pellet was then filtered through a 40-μm cell strainer, removing any tissue segments that failed to disassociate during collagenase treatment. To filter out cell types other than ventricular cardiomyocytes, we made use of differences in cell adhesion times using a 1.5-hour preplating step to preferentially select against rapidly adherent cell types, such as fibroblasts and endothelial cells. The supernatant was then recovered, isolating ventricular cardiomyocytes, which were concentrated an additional time using centrifugation, before counting the total number of NRVMs isolated and seeding onto biohybrid fins.

To fabricate the biohybrid swimmers, NRVMs were seeded at a density of 2.0 to 4.0 × 10^6 cells/cm^2. Samples were maintained in M199 medium containing 10% FBS for the first day before switching to M199 medium containing 2% (v/v) FBS after 2 days in culture. After that, the medium was exchanged every 2 days, and all experiments were performed between days 5 and 7 of culture. During incubation, all samples were maintained at 37°C, with 5% CO_2, in a humid environment.

Manufacturing biohybrid minirays

To prepare biohybrid ray models, glass microscope slides were first laser cut using a laser engraver (Minihelix Epilog Laser, Golden, CO) into ~28 mm–by–30 mm rectangular substrates. To form the spinal column, an ~50-μm groove was then etched into the substrate (3× 5% speed, 5% power, 500-Hz raster). Next, a sacrificial layer was applied, containing poly(*N*-isopropylacrylamide) dissolved in 1-butanol in a 1:100 (w/v) ratio, which was spun-coated onto the glass substrate at 4000 rpm for 1.5 min. To fabricate the neutrally buoyant polymeric body, a PDMS blend was used, containing a 1.6:1 ratio of soft (Sylgard 527, Dow Corning) and stiff (Sylgard 184, Dow Corning) PDMS. This was freshly prepared just before spinning, applying 1.5 ml of the PDMS blend to each substrate, before spin coating at 1500 rpm for 5 min. Substrates were then cured overnight at 45 °C, and the corresponding fin morphologies were cut using a laser engraver (4× 4% speed, 3% power, 2600-Hz raster).

Microcontact printing was then used to produce controlled FN patterning. To achieve this, photolithographic masks containing line patterns (20-μm width, with 10-μm gaps) were used as a template. SU-8 2010 photoresist (MicroChem Corp) was spun-coated onto silicon wafers (Wafer World), and a custom-built mask aligner was used to position the photolithographic mask. Samples were then exposed to ultraviolet (UV) radiation and submerged in propylene glycol methyl ether acetate to dissolve the non–photocrosslinked regions. The resulting wafer was then used as a template for producing patterned PDMS stamps (Sylgard 184, Dow Corning). After manufacturing, stamps were coated with human FN (25 μg/ml; BD Biosciences) in phosphate-buffered saline (PBS) for 45 min and were then air-dried to remove aqueous residue. Immediately before stamping, biohybrid ray substrates were treated in a UV-ozone cleaner (JetLight Company Inc.) for at least 8 min. Stamps were then inverted and placed onto the MTF substrates to transfer protein with the exposed line patterns. For biohybrid rays, this consisted of a 30° angled zig-zag or chevron pattern.

Generating ray morphologies using a genetic algorithm

To generate a variety of ray morphologies, a genetic algorithm was used (fig. S1), which was inspired by protein combinatorics. This defined sets of cubic Bézier curves as basis functions that can be combined to create a single fin geometry, allowing basis functions to be swapped in and out in a manner similar to amino acid sequences. This enabled a genetic evolution approach to be applied to each ray's geometry (as opposed to minor tweaks of continuous values), such that individual basis contributions could be scored and so that they would have to compete against one another to form a final morphology. Here, individual cubic Bézier curves, $B(t)$, were given by

$$B(t) = (1-t)^3 P_0 + 3(1-t)^2 t P_1 + 3(1-t)t^2 P_2 + t^3 P_3, \quad 0 \le t \le 1 \quad (4)$$

where P_0 to $P_4$are a set of control points in real space guiding the curve and t is a parametric unit defining a distance along the curve. For this genetic algorithm, cubic Bézier curves were selected because they provide the following set of useful features. First, by fixing both control points P_0 and P_4 at the x,y coordinates [0,0] and [1,0], respectively, this ensured that the resulting morphology would always form a closed shape when reflected about the x axis. This prevented bifurcation during ray manufacture and simulation. Second, by modulating control points P_2 and P_3, a multitude of shapes could be generated using only simple geometric perturbations, such as transposing $P_{2,[0,0]} \rightarrow P_{2,[1,0]}$. This meant that using simple geometric rules could provide a variety of morphological features,

emulating the emergence of macroscopic tissue structures from random initial configuration (fig. S1C). This allowed this algorithm to go from random initial shapes to pelagic fin–like structures by selecting combinations of basis functions with successively greater contributions to swimming velocity.

Next, ray geometries were formed from different combinations of Bézier curves. These basis functions were each assigned a letter (A to N), with B to M representing individual shapes, A representing an increase in the AR (chord span) and N representing a decrease in the AR. To form a given ray geometry, individual basis functions were then combined in a weighted sequence, with earlier basis functions being provided preference over later basis functions. This was used to emulate protein dynamics, where some mutations can lead to large changes in protein structure, with other mutations resulting in only minor tweaks to a protein's function/shape. The weighted contribution of each individual basis function, W_i, was given as

$$W_i = \frac{\left(2 - \frac{2i}{\mathrm{sDNA}_{\#}}\right)}{\left(\mathrm{sDNA}_{\#} + 1\right)} \tag{5}$$

where i is the index position of the basis function and $\mathrm{sDNA}_{\#}$ is the total number of basis functions included in an individual sequence. This provides basis functions near the front a greater contribution than basis functions near the rear. So that geometries could encode for both the shape and AR separately, the weights that basis functions provided to ARs (A and N) were determined in reverse order (such that A at the end of a sequence had greater weight than at the beginning). This meant that trade-offs still needed to be made between individual base pairs for a given morphology but that contributions to the AR could be competed for separately.

To compute the total fin shape, $F_s(t)$, basis functions were then combined such that

$$F_s(t) = \sum_i B_i(t) \cdot W_i \tag{6}$$

where $B_i(t)$is the basis function in the ith index slot. This provided a shape for each specific basis function sequence, such that DBG would be distinct from DGB or BGD, for instance. Last, to normalize the total surface area of each fin, a Riemann sum was used to approximate the integral of the surface area. Fin shape was then scaled linearly in both the x and y directions to preserve relative geometries and produce a normalized surface area (~15 mm^2), with the scaling factor determined numerically using Newton's method. Last, in the current study, we limited our fin morphologies to combinations of 14 basis functions in six possible slots. This resulted in a large configuration space (14^6–2) that served as a compromise between forming a continuous function out of fin morphology and "searchability" by limiting the total number of possible configurations.

Fin thin-film kinematics model

To describe the motion of the films during contraction, we constructed a kinematic model on the basis of three assumptions. The first assumption, that an MTF's curvature and shape can be described using Stoney's equation for anisotropic thin-film bilayer deformation, implies that contraction occurs along given cylinders in space. This describes the total motion of perpendicularly aligned ($\alpha = 0°$) thin films well and describes the initial motion of angled thin films ($\alpha < 0°$) but does not account for undulatory motions. Second, to account for this type of relaxation, we assumed that the cantilever's bending state can be expressed as a weighted average of the anisotropic and isotropic contraction states at any given time, with weights being determined by a transfer function. Last, to account for the resulting discrepancies in contractile strength, we assumed that the radius of cantilever curvature scales proportionally to the contractile area. Using these three assumptions provided a computationally efficient model for approximating thin-film kinematics. See the Supplementary Materials for a more detailed description.

LBM model assumptions

Ray fluid dynamic simulations were performed in a rectangular box with the dimensions 18 mm by 12 mm by 12 mm and a grid spacing of 0.125 mm, periodic boundary conditions for the inlet and outlet, and Dirichlet boundary condition assumed for the remaining sidewalls. For numeric stability, an initial fluid density of unity (one) was assumed, with a kinematic viscosity of 0.714 to simulate Tyrode's solution, and a Re of 60 was assumed. This was based on the size of the fabricated thin film, and the experimentally observed average fluid velocity propelled by the stationary fins. In total, for each thin film, 24 s was simulated (~14,400 time steps), with thin-film kinematics being simulated at a rate of 60 frames per second (16.6-ms time steps), whereas fluid dynamics were simulated at a rate of 600 Hz (1.66-ms time steps). These differences in stimulation rates allowed velocity information to propagate out from the film surface, more closely approximating a continuous time function. Thin films were simulated with a radius of curvature of 8 and 1.4 mm during diastole and systole, respectively, with a contractile angle $\alpha = 30°$. To ensure that thin films were capable of transferring momentum, films were assumed to have a thickness of double the grid spacing (0.25 mm). This was ~10× their actual thickness but was treated as if the films had a compensatorily reduced elastic modulus. Ray morphologies were simulated with a scaling factor of 4.0 mm, resulting in a maximum fin length of ~10 mm. Numerical calculations were performed using TensorFlow (v2.0.0) for graphical processing unit acceleration on a NVIDIA GTX 1080. Present LBM implementation was initially on the basis of Hennigh's LatFlow library (https://github.com/loliverhennigh/Lattice-Boltzmann-fluid-flow-in-Tensorflow).

NN model

The NN model was constructed using keras (v2.2.4-tf) with TensorFlow (v2.0.0) as a backend. Input swimmer configurations were one hot encoded as 6-by-4 arrays. Outputs were single node, cumulative density functions, with the loss function consisting of the sum of the mean absolute percentage error of these two output nodes. Two outputs in total were trained. The primary output was used to make predictions about the rank of each configuration. The second output, which was discarded outside of training, ensured that the sparse dense network continued to encode for a first-order approximation of each basis function's contribution to swimming speed. Optimization was performed using stochastic gradient descent (adam optimizer, learning rate = 0.001, and $\varepsilon = 1 \times 10^{-7}$, where ε is a small constant introduced during gradient descent to promote numerical stability). Dense networks used rectified line units (ReLu) as an activation function, until the final node, which used a sigmoidal activation function. For training, dropout layers (15%) were included between each dense/convolutional layer, with a global max pooling layer added before the final set of dense layers (see fig. S15A for the network architecture). The final model consisted of ~18,000 trainable parameters.

Statistical analysis

Unless otherwise noted, all error bars given as the SEM. Unless otherwise noted, all claims of statistical significance were based on a two-tailed Student's *t* test assuming equal variance, with confidence intervals of less than 5% being considered statistically significant (P value < 0.05).

Supplementary Materials

The PDF file includes:

Methods
Figs. S1 to S24
Tables S1 to S3
Legends for movies S1 to S10
References (*62*–*73*)

Other Supplementary Material for this manuscript includes the following:

Movies S1 to S10
MDAR Reproducibility Checklist

REFERENCES AND NOTES

1. M. Gazzola, M. Argentina, L. Mahadevan, Scaling macroscopic aquatic locomotion. *Nat. Phys.* **10**, 758–761 (2014).
2. S.-J. Park, M. Gazzola, K. S. Park, S. Park, V. Di Santo, E. L. Blevins, J. U. Lind, P. H. Campbell, S. Dauth, A. K. Capulli, F. S. Pasqualini, S. Ahn, A. Cho, H. Yuan, B. M. Maoz, R. Vijaykumar, J.-W. Choi, K. Deisseroth, G. V. Lauder, L. Mahadevan, K. K. Parker, Phototactic guidance of a tissue-engineered soft-robotic ray. *Science* **353**, 158–162 (2016).
3. L. Ricotti, B. Trimmer, A. W. Feinberg, R. Raman, K. K. Parker, R. Bashir, M. Sitti, S. Martel, P. Dario, A. Menciassi, Biohybrid actuators for robotics: A review of devices actuated by living cells. *Sci. Robot.* **2**, eaaq0495 (2017).
4. R. Raman, Biofabrication of living actuators. *Annu. Rev. Biomed. Eng.* **26**, 223–245 (2024).
5. M. Guix, R. Mestre, T. Patiño, M. de Corato, J. Fuentes, G. Zarpellon, S. Sánchez, Biohybrid soft robots with self-stimulating skeletons. *Sci. Robot.* **6**, eabe7577 (2021).
6. R. Raman, C. Cvetkovic, S. G. M. Uzel, R. J. Platt, P. Sengupta, R. D. Kamm, R. Bashir, Optogenetic skeletal muscle-powered adaptive biological machines. *Proc. Natl. Acad. Sci. U.S.A.* **113**, 3497–3502 (2016).
7. P. W. Alford, A. W. Feinberg, S. P. Sheehy, K. K. Parker, Biohybrid thin films for measuring contractility in engineered cardiovascular muscle. *Biomaterials* **31**, 3613–3621 (2010).
8. R. Raman, L. Grant, Y. Seo, C. Cvetkovic, M. Gapinske, A. Palasz, H. Dabbous, H. Kong, P. P. Pinera, R. Bashir, Damage, healing, and remodeling in optogenetic skeletal muscle bioactuators. *Adv. Healthc. Mater.* **6**, 1700030 (2017).
9. F. E. Fish, Limits of nature and advances of technology: What does biomimetics have to offer to aquatic robots? *Appl. Bionics Biomech.* **3**, 49–60 (2006).
10. D. T. Roper, S. Sharma, R. Sutton, P. Culverhouse, A review of developments towards biologically inspired propulsion systems for autonomous underwater vehicles. *Proc. Inst. Mech. Eng. H.* **225**, 77–96 (2011).
11. C. Laschi, B. Mazzolai, M. Cianchetti, Soft robotics: Technologies and systems pushing the boundaries of robot abilities. *Sci. Robot.* **1**, eaah3690 (2016).
12. N. C. Aschliman, M. Nishida, M. Miya, J. G. Inoue, K. M. Rosana, G. J. P. Naylor, Body plan convergence in the evolution of skates and rays (Chondrichthyes: Batoidea). *Mol. Phylogenet. Evol.* **63**, 28–42 (2012).
13. L. J. Rosenberger, Pectoral fin locomotion in batoid fishes: Undulation versus oscillation. *J. Exp. Biol.* **204**, 379–394 (2001).
14. J. C. Nawroth, H. Lee, A. W. Feinberg, C. M. Ripplinger, M. L. McCain, A. Grosberg, J. O. Dabiri, K. K. Parker, A tissue-engineered jellyfish with biomimetic propulsion. *Nat. Biotechnol.* **30**, 792–797 (2012).
15. K. Y. Lee, S.-J. Park, D. G. Matthews, S. L. Kim, C. A. Marquez, J. F. Zimmerman, H. A. M. Ardoña, A. G. Kleber, G. V. Lauder, K. K. Parker, An autonomously swimming biohybrid fish designed with human cardiac biophysics. *Science* **375**, 639–647 (2022).
16. H. Lipson, J. B. Pollack, Automatic design and manufacture of robotic lifeforms. *Nature* **406**, 974–978 (2000).
17. J. Hiller, H. Lipson, Automatic design and manufacture of soft robots. *IEEE Trans. Robot.* **28**, 457–466 (2012).
18. S. Kriegman, D. Blackiston, M. Levin, J. Bongard, Kinematic self-replication in reconfigurable organisms. *Proc. Natl. Acad. Sci. U.S.A.* **118**, e2112672118 (2021).
19. S. Kriegman, D. Blackiston, M. Levin, J. Bongard, A scalable pipeline for designing reconfigurable organisms. *Proc. Natl. Acad. Sci. U.S.A.* **117**, 1853–1859 (2020).
20. A. Menzer, Y. Gong, F. E. Fish, H. Dong, Bio-inspired propulsion: Towards understanding the role of pectoral fin kinematics in manta-like swimming. *Biomimetics* **7**, 45 (2022).
21. X. Liu, T. Iwasaki, F. Fish, Dynamic modeling and gait analysis of batoid swimming, in *2013 American Control Conference* (IEEE, 2013), pp. 566–571.
22. M. I. Lamas, C. G. Rodriguez, Hydrodynamics of biomimetic marine propulsion and trends in computational simulations. *J. Mar. Sci. Eng.* **8**, 479 (2020).
23. W. M. Van Rees, M. Gazzola, P. Koumoutsakos, Optimal shapes for anguilliform swimmers at intermediate Reynolds numbers. *J. Fluid Mech.* **722**, R3 (2013).
24. N. Hansen, S. D. Müller, P. Koumoutsakos, Reducing the time complexity of the derandomized evolution strategy with covariance matrix adaptation (CMA-ES). *Evol. Comput.* **11**, 1–18 (2003).
25. E. Brochu, V. M. Cora, N. de Freitas, A tutorial on Bayesian optimization of expensive cost functions, with application to active user modeling and hierarchical reinforcement learning. arXiv:1012.2599 [cs.LG] (2010).
26. C. Nyshadham, M. Rupp, B. Bekker, A. V. Shapeev, T. Mueller, C. W. Rosenbrock, G. Csányi, D. W. Wingate, G. L. W. Hart, Machine-learned multi-system surrogate models for materials prediction. *NPJ Comput. Mater.* **5**, 51 (2019).
27. B. J. Befort, R. S. DeFever, G. M. Tow, A. W. Dowling, E. J. Maginn, Machine learning directed optimization of classical molecular modeling force fields. *J. Chem. Inf. Model.* **61**, 4400–4414 (2021).
28. T. Klucznik, B. Mikulak-Klucznik, M. P. McCormack, H. Lima, S. Szymkuć, M. Bhowmick, K. Molga, Y. Zhou, L. Rickershauser, E. P. Gajewska, A. Toutchkine, P. Dittwald, M. P. Startek, G. J. Kirkovits, R. Roszak, A. Adamski, B. Sieredzińska, M. Mrksich, S. L. J. Trice, B. A. Grzybowski, Efficient syntheses of diverse, medicinally relevant targets planned by computer and executed in the laboratory. *Chem* **4**, 522–532 (2018).
29. K. T. Butler, D. W. Davies, H. Cartwright, O. Isayev, A. Walsh, Machine learning for molecular and materials science. *Nature* **559**, 547–555 (2018).
30. G. X. Gu, C.-T. Chen, D. J. Richmond, M. J. Buehler, Bioinspired hierarchical composite design using machine learning: simulation, additive manufacturing, and experiment. *Mater. Horiz.* **5**, 939–945 (2018).
31. P. Opgenorth, Z. Costello, T. Okada, G. Goyal, Y. Chen, J. Gin, V. Benites, M. de Raad, T. R. Northen, K. Deng, S. Deutsch, E. E. K. Baidoo, C. J. Petzold, N. J. Hillson, H. Garcia Martin, H. R. Beller, Lessons from two design–build–test–learn cycles of dodecanol production in *Escherichia coli* aided by machine learning. *ACS Synth. Biol.* **8**, 1337–1351 (2019).
32. K. K. Yang, Z. Wu, F. H. Arnold, Machine-learning-guided directed evolution for protein engineering. *Nat. Methods* **16**, 687–694 (2019).
33. C. Norn, B. I. M. Wicky, D. Juergens, S. Liu, D. Kim, D. Tischer, B. Koepnick, I. Anishchenko, F. Players, D. Baker, S. Ovchinnikov, Protein sequence design by conformational landscape optimization. *Proc. Natl. Acad. Sci. U.S.A.* **118**, e2017228118 (2021).
34. K. C. Hall, P. J. Hundt, J. D. Swenson, A. P. Summers, K. D. Crow, The evolution of underwater flight: The redistribution of pectoral fin rays, in manta rays and their relatives (Myliobatidae). *J. Morphol.* **279**, 1155–1170 (2018).
35. J. E. Fontanella, F. E. Fish, E. I. Barchi, R. Campbell-Malone, R. H. Nichols, N. K. DiNenno, J. T. Beneski, Two- and three-dimensional geometries of batoids in relation to locomotor mode. *J. Exp. Mar. Biol. Ecol.* **446**, 273–281 (2013).
36. F. E. Fish, H. Dong, J. J. Zhu, H. Bart-Smith, Kinematics and hydrodynamics of mobuliform swimming: Oscillatory winged propulsion by large pelagic batoids. *Mar. Technol. Soc. J.* **51**, 35–47 (2017).
37. A. W. Feinberg, A. Feigel, S. S. Shevkoplyas, S. Sheehy, G. M. Whitesides, K. K. Parker, Muscular thin films for building actuators and powering devices. *Science* **317**, 1366–1370 (2007).
38. J. Shim, A. Grosberg, J. C. Nawroth, K. Kit Parker, K. Bertoldi, Modeling of cardiac muscle thin films: Pre-stretch, passive and active behavior. *J. Biomech.* **45**, 832–841 (2012).
39. A. W. Feinberg, P. W. Alford, H. Jin, C. M. Ripplinger, A. A. Werdich, S. P. Sheehy, A. Grosberg, K. K. Parker, Controlling the contractile strength of engineered cardiac muscle by hierarchal tissue architecture. *Biomaterials* **33**, 5732–5741 (2012).
40. E. G. Drucker, J. A. Walker, M. W. Westneat, Mechanics of pectoral fin swimming in fishes, in *Evolutionary Computation*, R. E. Shadwick, G. V. Lauder, Eds. (Academic Press, 2005), vol. 23, pp. 369–423.
41. A. Grosberg, P. W. Alford, M. L. McCain, K. K. Parker, Ensembles of engineered cardiac tissues for physiological and pharmacological study: Heart on a chip. *Lab Chip* **11**, 4165–4173 (2011).
42. D. A. Perumal, A. K. Dass, A review on the development of lattice Boltzmann computation of macro fluid flows and heat transfer. *Alex. Eng. J.* **54**, 955–971 (2015).
43. K. Suzuki, K. Minami, T. Inamuro, Lift and thrust generation by a butterfly-like flapping wing–body model: Immersed boundary–lattice Boltzmann simulations. *J. Fluid Mech.* **767**, 659–695 (2015).
44. A. N. Gorban, D. J. Packwood, Enhancement of the stability of lattice Boltzmann methods by dissipation control. *Phys. A: Stat. Mech. Appl.* **414**, 285–299 (2014).
45. C. Chang, C.-H. Liu, C.-A. Lin, Boundary conditions for lattice Boltzmann simulations with complex geometry flows. *Comput. Math. Appl.* **58**, 940–949 (2009).
46. N. Thürey, K. Iglberger, U. Rüde, Free surface flows with moving and deforming objects for LBM. *Proc. Vis. Model. Vis.* **2006**, 193–200 (2006).

47. K. Hornik, M. Stinchcombe, H. White, Multilayer feedforward networks are universal approximators. *Neural Netw.* **2**, 359–366 (1989).
48. M. Leshno, V. Y. Lin, A. Pinkus, S. Schocken, Multilayer feedforward networks with a nonpolynomial activation function can approximate any function. *Neural Netw.* **6**, 861–867 (1993).
49. F. H. Arnold, Design by directed evolution. *Acc. Chem. Res.* **31**, 125–131 (1998).
50. A. Hansen, The three extreme value distributions: An introductory review. *Front. Phys.* **8**, 604053 (2020).
51. P. W. Webb, V. De Buffrénil, Locomotion in the biology of large aquatic vertebrates. *Trans. Am. Fish. Soc.* **119**, 629–641 (1990).
52. D. E. Sasko, M. N. Dean, P. J. Motta, R. E. Hueter, Prey capture behavior and kinematics of the Atlantic cownose ray, *Rhinoptera bonasus*. *Zoology* **109**, 171–181 (2006).
53. S. Mulvany, P. J. Motta, The morphology of the cephalic lobes and anterior pectoral fins in six species of batoids. *J. Morphol.* **274**, 1070–1083 (2013).
54. F. E. Fish, A. Kolpas, A. Crossett, M. A. Dudas, K. W. Moored, H. Bart-Smith, Kinematics of swimming of the manta ray: Three-dimensional analysis of open-water maneuverability. *J. Exp. Biol.* **221**, jeb166041 (2018).
55. B. Jensen, T. Wang, V. M. Christoffels, A. F. M. Moorman, Evolution and development of the building plan of the vertebrate heart. *Biochim. Biophys. Acta* **1833**, 783–794 (2013).
56. A. Stephenson, J. W. Adams, M. Vaccarezza, The vertebrate heart: An evolutionary perspective. *J. Anat.* **231**, 787–797 (2017).
57. C. J. Mandrycky, N. P. Williams, I. Batalov, D. El-Nachef, B. S. de Bakker, J. Davis, D.-H. Kim, C. A. DeForest, Y. Zheng, K. R. Stevens, N. J. Sniadecki, Engineering heart morphogenesis. *Trends Biotechnol.* **38**, 835–845 (2020).
58. M. V. Sherrid, J. Männer, D. G. Swistel, I. Olivotto, D. G. Halpern, On the cardiac loop and its failing: Left ventricular outflow tract obstruction. *J. Am. Heart Assoc.* **9**, e014857 (2020).
59. A. Lee, A. R. Hudson, D. J. Shiwarski, J. W. Tashman, T. J. Hinton, S. Yerneni, J. M. Bliley, P. G. Campbell, A. W. Feinberg, 3D bioprinting of collagen to rebuild components of the human heart. *Science* **365**, 482–487 (2019).
60. E. Mirdamadi, J. W. Tashman, D. J. Shiwarski, R. N. Palchesko, A. W. Feinberg, FRESH 3D bioprinting a full-size model of the human heart. *ACS Biomater. Sci. Eng.* **6**, 6453–6459 (2020).
61. H. Chang, Q. Liu, J. F. Zimmerman, K. Y. Lee, Q. Jin, M. M. Peters, M. Rosnach, S. Choi, S. L. Kim, H. A. M. Ardoña, L. A. MacQueen, C. O. Chantre, S. E. Motta, E. M. Cordoves, K. K. Parker, Recreating the heart's helical structure-function relationship with focused rotary jet spinning. *Science* **377**, 180–185 (2022).
62. S. S. Garud, I. A. Karimi, M. Kraft, Design of computer experiments: A review. *Comput. Chem. Eng.* **106**, 71–95 (2017).
63. A. Liberzon, D. Lasagna, M. Aubert, P. Bachant, Jakirkham, Ranleu, Tomerast, T. Käufer, J. Borg, C. Dallas, B. Vodenicharski, OpenPIV/openpiv-python: Fixed windows conda-forge failure with encoding (Zenodo, 2019).
64. F. Noca, D. Shiels, D. Jeon, A comparison of methods for evaluating time-dependent fluid dynamic forces on bodies, using only velocity fields and their derivatives. *J. Fluids Struct.* **13**, 551–578 (1999).
65. W. Chae, Y. Cha, S. D. Peterson, M. Porfiri, Flow measurement and thrust estimation of a vibrating ionic polymer metal composite. *Smart Mater. Struct.* **24**, 095018 (2015).
66. C. Prince, W. Lin, J. Lin, S. D. Peterson, M. Porfiri, Temporally resolved hydrodynamics in the vicinity of a vibrating ionic polymer metal composite. *J. Appl. Phys.* **107**, 094908 (2010).
67. S. D. Peterson, M. Porfiri, A. Rovardi, A particle image velocimetry study of vibrating ionic polymer metal composites in aqueous environments. *IEEE/ASME Trans. Mechatron.* **14**, 474–483 (2009).
68. K. N. Lucas, G. V. Lauder, E. D. Tytell, Airfoil-like mechanics generate thrust on the anterior body of swimming fishes. *Proc. Natl. Acad. Sci. U.S.A.* **117**, 10585–10592 (2020).
69. J. O. Dabiri, S. Bose, B. J. Gemmell, S. P. Colin, J. H. Costello, An algorithm to estimate unsteady and quasi-steady pressure fields from velocity field measurements. *J. Exp. Biol.* **217**, 331–336 (2014).
70. G. G. Stoney, The tension of metallic films deposited by electrolysis. *Proc. R. Soc. Lond. A* **82**, 172–175 (1909).
71. X. Feng, Y. Huang, A. J. Rosakis, On the Stoney formula for a thin film/substrate system with nonuniform substrate thickness. *J. Appl. Mech.* **74**, 1276–1281 (2007).
72. J. Pinnell, S. Turner, S. Howell, Cardiac muscle physiology. *Contin. Educ. Anaesth. Crit. Care Pain* **7**, 85–88 (2007).
73. H. Aono, A. Gupta, D. Qi, W. Shyy, The lattice Boltzmann method for flapping wing aerodynamics, in *40th Fluid Dynamics Conference* (AIAA, 2010), pp. 1–27.

Acknowledgments: We would like to thank A.G. Kleber for discussions regarding cardiac physiology, J. Alexander for continued support of the project, H. Pimentel and M. Rosnach for the help in photographing live rays, and O. Hennigh for allowing the use of his initial implementation of the LBM LatFlow library. **Funding:** This work was sponsored in part by NTT Research Inc., the John A. Paulson School of Engineering and Applied Sciences at Harvard University, the Wyss Institute for Biologically Inspired Engineering at Harvard University, the Harvard Materials Research Science and Engineering Center (DMR-1420570 and DMR-2011754), and the Center for Nanoscale Systems, a member of the National Nanotechnology Coordinated Infrastructure (NNCI), which is supported by the National Science Foundation (1541959). In addition, J.F.Z. thanks the National Institutes of Health (NIH) for support through the National Research Service Award fellowship program (T32 HL007572). H.A.M.A. thanks the American Chemical Society for support through the Irving S. Sigal Postdoctoral Fellowship. The content is solely the responsibility of the authors and does not necessarily represent the official views of NTT Research Inc. or the NIH. The authors confirm that these parties had no influence on the study design, contents of the article, or selection of this journal. **Author contributions:** J.F.Z., D.J.D., and K.K.P. designed the study. J.F.Z. and J.I. performed the cell culture and built the biohybrid robotics. J.F.Z. and D.J.D. developed the machine learning and simulation software. J.F.Z. performed the data analysis. J.F.Z., Q.J., H.A.M.A, R.I., and S.L.K. performed animal protocols to obtain cardiomyocytes. K.K.P. supervised the research. All authors discussed the results and contributed to the writing of the final manuscript. **Competing interests:** The authors declare that they have no conflict of interest. **Data and materials availability:** All data necessary to understand and assess the conclusions are available in the main text or in Supplementary Materials. Source code is available via Zenodo (10.5281/zenodo.14619232), or the latest version is at https://github.com/SeasDBG/BiohybridRays.

Submitted 10 July 2024
Accepted 14 January 2025
Published 12 February 2025
10.1126/scirobotics.adr6472

Science Robotics

Bioinspired design of a tissue-engineered ray with machine learning

John F. Zimmerman, Daniel J. Drennan, James Ikeda, Qianru Jin, Herdeline Ann M. Ardoña, Sean L. Kim, Ryoma Ishii, and Kevin Kit Parker

Sci. Robot. **10** (99), eadr6472. DOI: 10.1126/scirobotics.adr6472

Science Robotics (ISSN 2470-9476) is published by the American Association for the Advancement of Science. 1200 New York Avenue NW, Washington, DC 20005. The title *Science Robotics* is a registered trademark of AAAS.